



Measurement of local current density of all-vanadium redox flow batteries



Wen-Yen Hsieh ^a, Chih-Hsing Leu ^b, Chun-Hsing Wu ^b, Yong-Song Chen ^{a,*}

^a Advanced Institute of Manufacturing with High-tech Innovations and Department of Mechanical Engineering, National Chung Cheng University, 168 University Rd., Minhsiung Township, 62102 Chiayi, Taiwan, ROC

^b Green Energy and Environment Research Laboratories, Industrial Technology Research Institute, 195, Sec. 4, Chung Hsing Rd., Chutung, Hsinchu 31040, Taiwan, ROC

HIGHLIGHTS

- Local current density is measured by two specially designed single cells.
- Variations of local current density during charge/discharge process are presented.
- Effect of electrolyte flow rate on current density variation is shown.
- Lower limit of state of charge during discharge process is evaluated.

ARTICLE INFO

Article history:

Received 7 March 2014

Received in revised form

13 June 2014

Accepted 15 June 2014

Available online 21 June 2014

Keywords:

All-vanadium redox flow battery

Local current density

Electrolyte flow rate

Discharge capacity

ABSTRACT

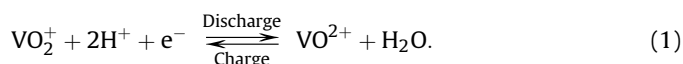
This article presents a preliminary study of the measurement of local current density in all-vanadium redox flow batteries. Two batteries are designed and manufactured in this study, and the experimental results are compared. In the first cell, the current collector is divided into 25 segments, and the flow field plate is not segmented, whereas in the other cell, the flow field plate is segmented. The effects of the electrolyte flow rate on the battery efficiencies and the local current density variation are investigated. The experimental results show that the current density near the outlet significantly decreases when the discharge capacity approaches zero. In addition, the battery has a larger discharge depth at a higher electrolyte flow rate.

© 2014 Elsevier B.V. All rights reserved.

1. Introduction

All-vanadium redox flow batteries (VRFBs) have garnered substantial attention over the past few years because of renewable energy storage requirements. A VRFB discharges and stores electricity through the redox reaction between vanadium ion oxidation states. In a VRFB system, V^{2+}/V^{3+} and V^{4+}/V^{5+} redox couples serve as the negative and positive electrolytes, respectively [1,2]. During discharge, V^{2+} is oxidized to V^{3+} , while V^{5+} is reduced to V^{4+} . In the charging process, these reactions proceed in the opposite direction.

At the positive electrode:



At the negative electrode:



Both the negative and positive electrolytes are stored in reservoirs outside the VRFB cell and are pumped into the cell stack during electrochemical reactions. Because of this, the energy capacity can be increased by simply adding more electrolytes to the reservoirs, and the output power is determined by the cell number and active area of the electrodes. Because the energy capacity is determined by the amount of electrolyte stored in the reservoirs and because the power output is determined by the cell stack, the power and energy of a VRFB system can be individually designed. Moreover, the positive and negative electrolytes are separately stored, resulting in low self-discharging. Because of these advantages over other energy storage systems, VRFB systems are considered potential candidates for large-scale energy storage and

* Corresponding author. Tel.: +886 5 272 0411x33309; fax: +886 5 272 0589.

E-mail address: imeysc@ccu.edu.tw (Y.-S. Chen).

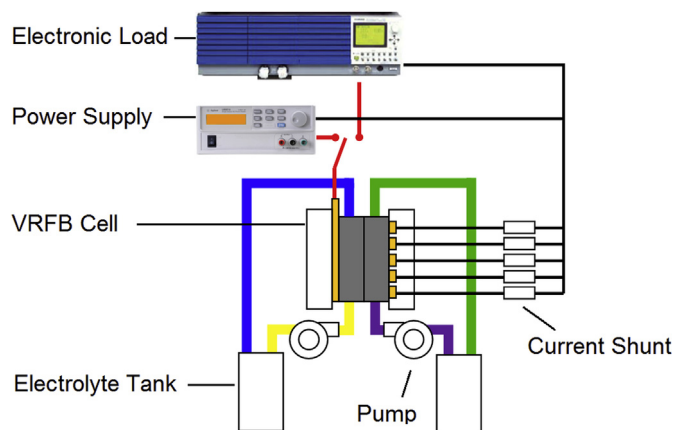


Fig. 1. A schematic of the experimental setup.

have been coupled to intermittent renewable power sources, such as solar or wind power systems [3–6]. In the coupled system, VRFB systems perform load leveling and peak shaving.

The major challenges for the commercialization of VRFBs are the key materials and system optimization, which significantly influence the efficiency of a VRFB system. Several studies have investigated the key materials, including electrolyte additives [7], sulfate–chloride mixed electrolytes [8], carbon paper electrode coated with supported tungsten trioxide [9], and modified separators [10–17], but few have focused on the system efficiency [18–20].

Ma et al. [18] experimentally studied the effect of the electrolyte flow rate on the performance of VRFBs operating at different current densities and proposed an optimal strategy for the electrolyte flow rate. They suggested that at each operating current density, the electrolytes should be supplied with either low or high flow rates, depending on the cell voltage. Ma's

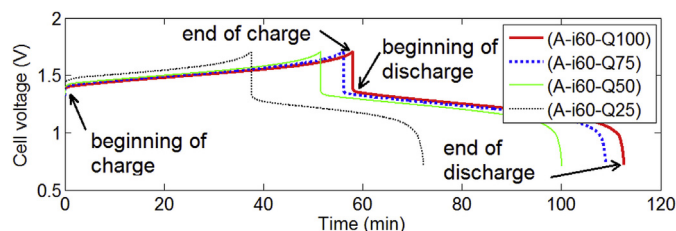


Fig. 3. Charge–discharge curves of cell A at 60 mA cm^{-2} .

experimental results also showed that the capacity and efficiency increased with increasing electrolyte flow rate. Benjamin et al. [19] compared the battery efficiencies determined using cutoff voltages and SOC limits. Tang et al. [20] modeled the concentration overpotential as a function of the electrolyte flow rate to investigate the effect of the electrolyte flow rate on battery efficiency. They suggested an optimized variable flow rate with a flow factor of 7.5, which resulted in higher system efficiencies over constant flow rates. When the electrolyte flow rate increased because of a low reactant concentration, the concentration overpotential was reduced. Although the effect of the electrolyte flow rate on cell performance has been studied, its effect on local current density has not been reported as far as we know.

In this study, two VRFB cells are designed for the measurement of local current density. The major difference in the design is the method of dividing the active area. The experimental results of the two designs are compared and discussed. The effect of the electrolyte flow rate on the current density distribution is also studied.

2. Experimental

The experimental setup, which consists of the VRFB single cell, electrolyte recirculation system, and the measurement system, is illustrated as Fig. 1.

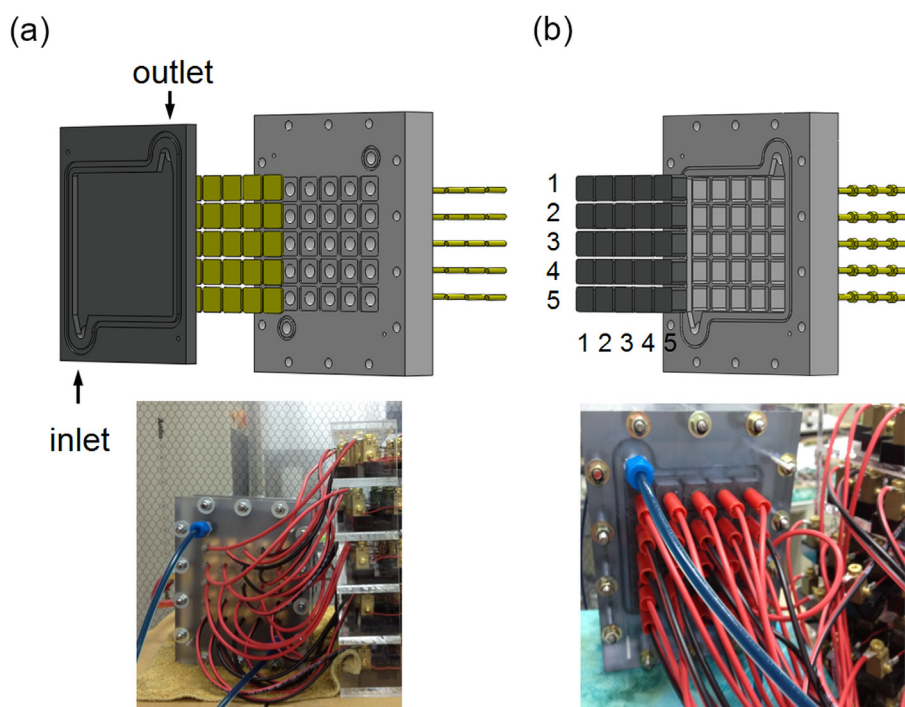


Fig. 2. Schematics and photos of the two cell designs used in this study. (a) Cell A: gold-plated current collector divided into 25 segments. (b) Cell B: graphite flow field plate divided into 25 segments.

Table 1
Efficiencies of cell A at 60 mA cm⁻².

Operating condition	CE (%)	VE (%)	EE (%)	DC (mAh ml ⁻¹)
(A-i60-Q25)	92.7	76.0	70.5	17.34
(A-i60-Q50)	94.6	79.0	74.7	24.28
(A-i60-Q75)	94.4	79.3	74.9	26.42
(A-i60-Q100)	94.3	80.0	75.5	27.31

2.1. VRFB single cell

In this study, we designed and manufactured two single cells with different structures for the local current density measurement. The current density distribution measurement technique for the two cells was similar. The active area of each cell was divided into 25 segments. Each segment was connected with a 50 mΩ current shunt.

For both of the two cells with an active area of 100 cm² (10 × 10 cm), a proton exchange membrane (Nafion 117, Dupont, USA) was employed as the separator. The porous electrodes (100 mm × 100 mm × 6 mm) were made of graphite felt (COS1011, CeTech, Taiwan). The major difference between these two cells is described below.

For cell A, the current collector of the negative side was replaced by 25 gold-coated copper segments (18 × 18 × 1 mm), as shown in Fig. 2(a). Each segment was soldered with a wire connected with a current shunt. To decrease the contact

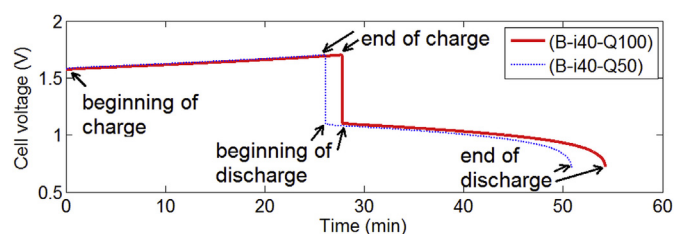


Fig. 5. Charge–discharge curves of cell B operated at 40 mA cm⁻².

Table 2
Efficiencies of cell B at 40 mA cm⁻².

Operating condition	CE (%)	VE (%)	EE (%)	DC (mAh ml ⁻¹)
(B-i40-Q50)	95.3	60.9	58.1	16.5
(B-i40-Q100)	94.5	61.5	58.1	17.7

resistance, a flexible graphite sheet was placed between the flow field plate and the 25 segments.

For cell B, a space (100 × 100 × 5 mm) for the porous electrode and the 25 holes (18 × 18 × 10 mm) for the graphite segments were machined on an end plate made of polyvinylchloride (PVC), as shown in Fig. 2(b). Each graphite segment was plugged with a banana connector. Sealant was applied between the graphite segments and the end plate to avoid leakage of the electrolyte.

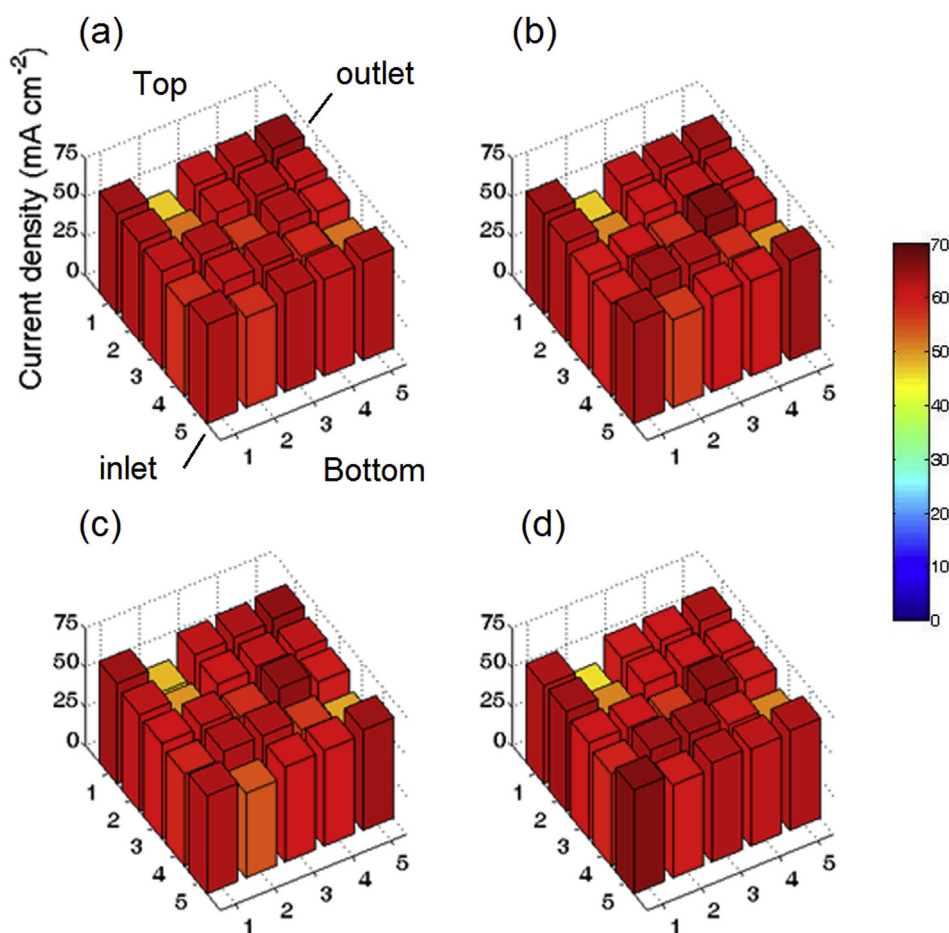


Fig. 4. Current density distributions of cell A at (a) the beginning of the charging process; (b) the end the charging process; (c) the beginning of the discharging process; and (d) the end of the discharging process. The operating condition is (A-i60-Q100).

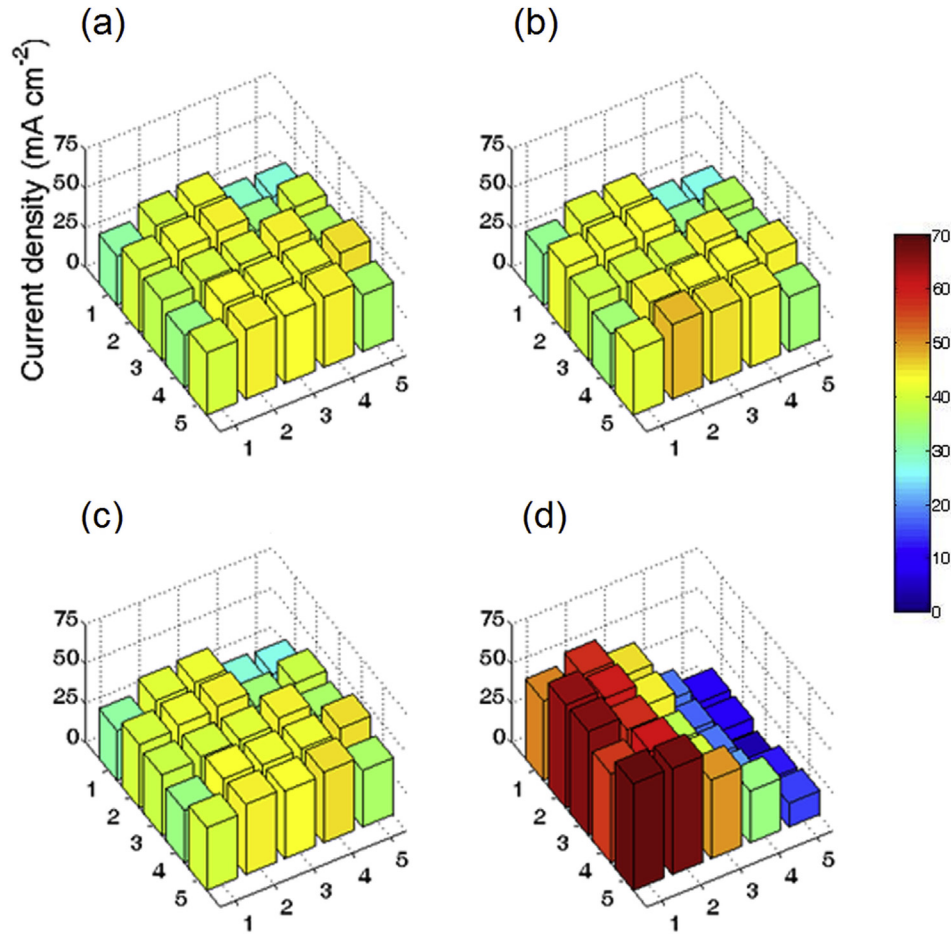


Fig. 6. Current density distributions of cell B at (a) the beginning of the charging process; (b) the end of the charging process; (c) the beginning of the discharging process; and (d) the end of the discharging process. The operating condition is (B-i40-Q50).

Both the inlets of the anode and cathode electrolytes were placed at the bottom left of the active area, and the outlets were placed at the top right, as indicated in Fig. 2(a). The inlet and outlet positions of both cells were the same. The numbers shown in Fig. 2(b) help indicate the position of the measured local current density.

2.2. Electrolyte system

The electrolyte was obtained by dissolving 1.5 M VOSO_4 in 2.0 M H_2SO_4 . The theoretical energy capacity is approximately 40 mA per ml of electrolyte. Both the positive and negative electrolyte reservoirs were initially filled with the V^{4+} solution. The positive electrolyte reservoir was initially 200 ml, while the negative side was 100 ml. In the first charging step, the V^{4+} in the electrolyte was converted to V^{5+} and V^{2+} for the positive and negative sides, respectively. Next, half of the positive electrolyte was removed to make the electrolyte volume in the two reservoirs equal. A continuous nitrogen flow was fed to the negative electrolyte reservoir to avoid oxidation of the V^{2+} . Two diaphragm pumps (SMART digital DDA7.5-16AR-PVC/V/C, Grundfos, Denmark) were employed to recirculate the positive and negative electrolytes between the reservoirs and the VRFB cell.

2.3. Measurement system

The VRFB cell was charged with a power supply (U8001A, Agilent, USA) and discharged using an electronic load

(PLZ664WA, Kikusui Electronics, Japan). The cell voltage and current were monitored and recorded using a data acquisition system (NI 9205, National Instrument, USA) for subsequent analysis.

2.4. Experimental procedure

The current density was recorded when the VRFB was operated with selected electrolyte flow rates and load currents. Both the charge and discharge current densities were the same and constant. At each current density, both the positive and negative electrolytes were delivered and recirculated with appropriate flow rates. Under each operating condition, the cell was charged and discharged between 0.7 and 1.7 V for three cycles, and the experimental data of the third cycle was used to calculate the battery efficiencies. The coulombic efficiency (CE), voltage efficiency (VE), energy efficiency (EE), and discharge capacity (DC) were calculated using the following equations, respectively:

$$\text{CE} = \frac{\int i_{\text{discharge}}(t) dt}{\int i_{\text{charge}}(t) dt} \quad (3)$$

$$\text{VE} = \frac{V_{\text{avg, discharge}}}{V_{\text{avg, charge}}} \quad (4)$$

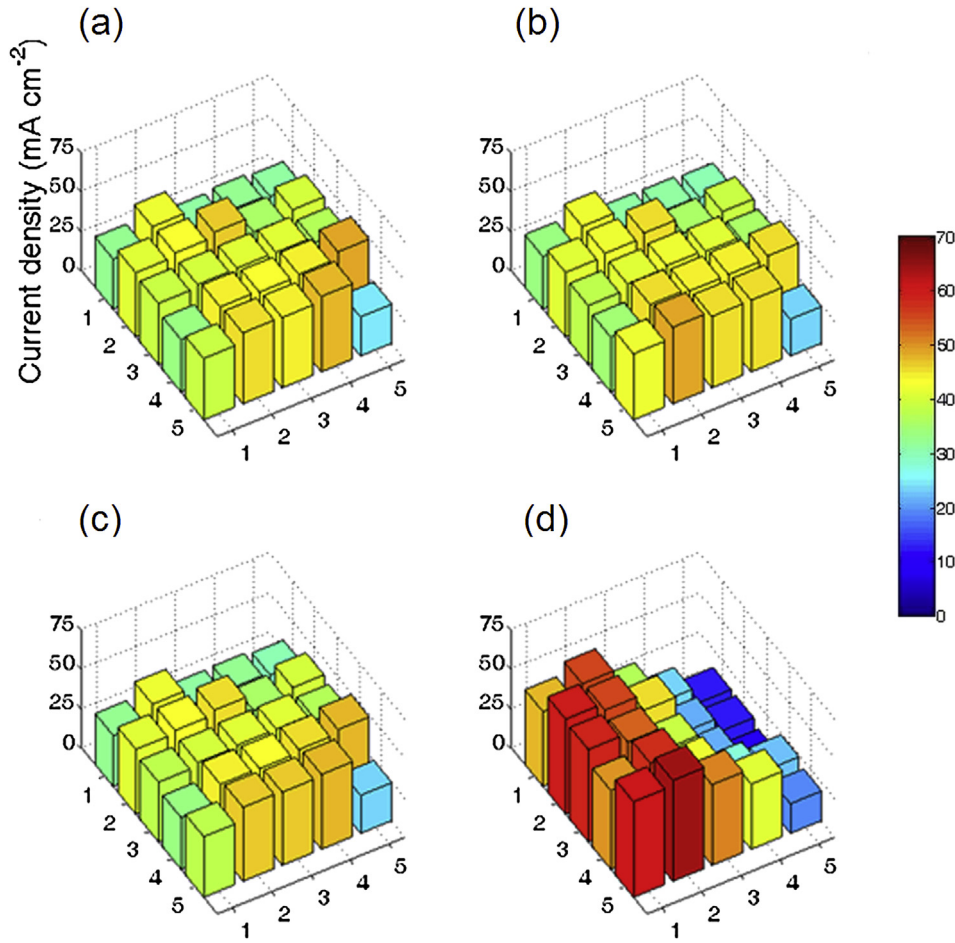


Fig. 7. Current density distributions of cell B at (a) the beginning of the charging process; (b) the end the charging process; (c) the beginning of the discharging process; and (d) the end of the discharging process. The operating condition is (B-i40-Q100).

$$EE = \frac{\int P_{VRB,discharge}(t)dt}{\int P_{VRB,charge}(t)dt} \quad (5)$$

$$DC = \int i_{discharge}(t)dt. \quad (6)$$

3. Results and discussion

Although the experimental results indicate that cell A is not suitable for the measurement of local current density, some data from cell A under selected operating conditions are presented and discussed. The operating conditions are described using the notation (A/B-i#-Q#), where A/B denotes cell A or B, i represents the current density in mA cm^{-2} , and Q is the electrolyte flow rate in ml min^{-1} .

3.1. Current density distribution of cell A

Fig. 3 shows the charge–discharge curves of cell A while operating at 60 mA cm^{-2} with four electrolyte flow rates: 25, 50, 75, and 100 ml min^{-1} . The battery efficiencies of cell A are compared in Table 1 based on the experimental data in Fig. 3. This shows that the

DC increases with increasing electrolyte flow rate. This tendency is similar to an ordinary VRFB [18]. Four selected snapshots of the current density distribution, corresponding to the marks in Fig. 3, are presented in Fig. 4.

Fig. 4(a)–(d) represents the current density distributions during the initial charging period, the final charging period, the initial discharging period, and the final discharging period, respectively. It can be seen that the current density distribution does not vary significantly with time. This may be caused by the contact resistances among the 25 segments not being equal, resulting from non-uniform compression pressure on each segment. As a result, the current density distribution is mainly affected by the contact resistance. Another possible reason is the in-plane current flow in the 5 mm-thick flow field plate, resulting in a redistribution of current density when current flows from the electrode side to the current-collector side through the flow field plate.

3.2. Current density distribution of cell B

Cell B is designed to eliminate the effects of the in-plane current flow on the current density distribution. The charge–discharge curves of cell B operated at 40 mA cm^{-2} are shown in Fig. 5, and the battery efficiencies are listed in Table 2. Compared to cell A, cell B shows significantly lower VE and DC. This may be because the contact resistance between the banana plug and graphite is higher than that between the current collectors and the graphite plate in cell A.

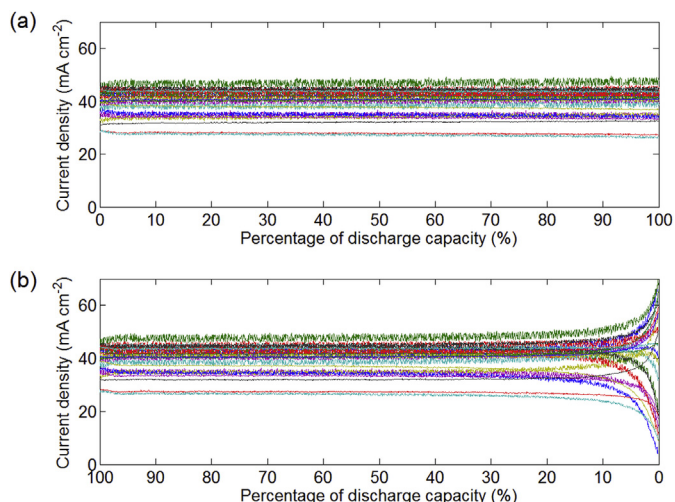


Fig. 8. Variations of the local current density with respect to the SOC of cell B operated at (B-i40-Q50) during the (a) charging and (b) discharging process.

Figs. 6 and 7 show the current density distributions of cell B operated under the conditions (B-i40-Q50) and (B-i40-Q100), respectively. Fig. 6(a) and (b) shows that during the charging process, no considerable variation in current density distribution is observed. However, at the end of discharging process, the current density close to the outlet decreases significantly as shown in Fig. 6(c) and (d). Because the concentration of V^{2+} (and V^{5+}) in the electrolyte is the lowest at the outlet, the local performance of the cell close to the outlet is the lowest. It can also be seen in Fig. 6(d) that at the end of discharging process, the local current density of the right half area of the cell is smaller than that of the left half. This may be attributed to the electrolyte flow distribution. In cell B, the inlet is placed lower than the bottom of the active area as depicted in Fig. 2(b). Most of the inflow electrolyte initially goes upward and then toward the right, resulting in a higher concentration of V^{2+} (and V^{5+}) in the left half of the cell. The electrolyte flow distribution can be improved through the flow field design of the frame [21]; however, its effect on current density distribution is not focused at current stage of this study.

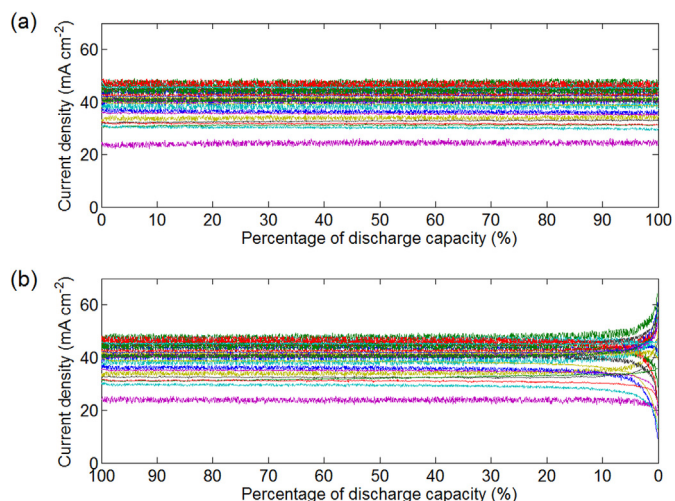


Fig. 9. Variations of the local current density with respect to the SOC of cell B operated at (B-i40-Q100) during the (a) charging and (b) discharging process.

Fig. 8 shows the variations of the local current density with respect to the DC of cell B operated under (B-i40-Q50) during the charging and discharging processes. During the charging process, the local current density exhibits a stable distribution; however, during the discharging process, a variation of the current density distribution occurs when the DC approaches approximately 20%. Furthermore, the local current density of a number of segments close to the outlet shows dramatic decreases at a DC of 10%. Some of them even approach zero. In contrast, the local current density of a number of segments close to the inlet increases during a galvanic discharge. It has been experimentally shown that the battery efficiency decreases with increasing current density. Thus, the lower limit of the DC during the discharging process can be determined as 10% under the operating condition (B-i40-Q50).

The variations of the local current density at an electrolyte flow rate of 100 ml min^{-1} are shown in Fig. 9. Fig. 9(b) suggests that the lower limit of the DC is approximately 5%. Equivalently, the discharge depth is increased by increasing the electrolyte flow rate. However, in contrast, higher electrolyte flow rates result in larger power consumptions by the pumps. Therefore, the effect of the electrolyte flow rate on the local current density distribution and the discharge depth must be evaluated to determine an optimal electrolyte flow rate. In the future, the effects of the electrode design on the local current density will be investigated using a newly designed cell.

4. Conclusion

To measure the current density distribution, two VRFB cells with an active area of 100 cm^2 were designed in this study. In the first cell, the gold-plated current collector of the negative side is divided into 25 segments. In the other cell, the positive and negative graphite flow field plates are divided into 25 segments. It is shown that the cell design significantly influences the experimental results. The accuracy of the measurement may be attributed to both the thickness of the flow field plates and the contact resistance. The second cell with divided graphite field plates exhibits a significant improvement in the measurement of the local current density. However, its performance decreases because of the increased contact resistance. The experimental results show that the current density close to the outlet significantly decreases when the DC approaches zero. Moreover, the discharge depth is larger at a higher electrolyte flow rate.

Acknowledgments

The authors would like to acknowledge the support from the National Science Council of Taiwan, ROC (102-ET-E-194-001-ET) and the Bureau of Energy, Ministry of Economic Affairs, Taiwan, ROC for this study.

References

- [1] M. Skyllas-Kazacos, G. Kazacos, G. Poon, H. Verseema, *Int. J. Energy Res.* 34 (2010) 182.
- [2] C. Sun, J. Chen, H. Zhang, X. Han, Q. Luo, *J. Power Sources* 195 (2010) 890.
- [3] C. Fabjan, J. Garche, B. Harrer, L. Jörissen, C. Kolbeck, F. Philipp, G. Tomazic, F. Wagner, *Electrochim. Acta* 47 (2001) 825.
- [4] L. Barote, C. Marinescu, in: 2009 Int. Conf. Clean Electr. Power, IEEE, 2009, p. 253.
- [5] F. Díaz-González, A. Sumper, O. Gomis-Bellmunt, R. Villafila-Robles, *Renew. Sustain. Energy Rev.* 16 (2012) 2154.
- [6] B. Turker, S. Arroyo Klein, E.-M. Hammer, B. Lenz, L. Komsijska, *Energy Convers. Manag.* 66 (2013) 26.
- [7] Z. Jia, B. Wang, S. Song, X. Chen, *J. Electrochem. Soc.* 159 (2012) A843.
- [8] L. Li, S. Kim, W. Wang, M. Vijayakumar, Z. Nie, B. Chen, J. Zhang, G. Xia, J. Hu, G. Graff, J. Liu, Z. Yang, *Adv. Energy Mater.* 1 (2011) 394.
- [9] C. Yao, H. Zhang, T. Liu, X. Li, Z. Liu, *J. Power Sources* 218 (2012) 455.

- [10] H. Zhang, H. Zhang, F. Zhang, X. Li, Y. Li, I. Vankelecom, *Energy Environ. Sci.* 6 (2013) 776.
- [11] H. Zhang, H. Zhang, X. Li, Z. Mai, J. Zhang, *Energy Environ. Sci.* 4 (2011) 1676.
- [12] C. Yao, H. Zhang, T. Liu, X. Li, Z. Liu, *J. Power Sources* 237 (2013) 19.
- [13] G. Hwang, H. Ohya, *J. Membr. Sci.* 120 (1996) 55.
- [14] G. Hwang, H. Ohya, *J. Membr. Sci.* 132 (1997) 55.
- [15] T. Sukkar, M. Skyllas-Kazacos, *J. Membr. Sci.* 222 (2003) 235.
- [16] T. Sukkar, M. Skyllas-Kazacos, *J. Membr. Sci.* 222 (2003) 249.
- [17] D. Chen, M.A. Hickner, E. Agar, E.C. Kumbur, *Electrochem. Commun.* 26 (2013) 37.
- [18] X. Ma, H. Zhang, C. Sun, Y. Zou, T. Zhang, *J. Power Sources* 203 (2012) 153.
- [19] A. Benjamin, E. Agar, C.R. Dennison, E.C. Kumbur, *Electrochem. Commun.* 35 (2013) 42.
- [20] A. Tang, J. Bao, M. Skyllas-Kazacos, *J. Power Sources* 248 (2014) 154.
- [21] S. Kim, E. Thomsen, G. Xia, Z. Nie, J. Bao, K. Recknagle, W. Wang, V. Viswanathan, Q. Luo, X. Wei, A. Crawford, G. Coffey, G. Maupin, V. Sprenkle, *J. Power Sources* 237 (2013) 300.